In-plane gradient-magnetic-field-induced vortex lattices in spin-orbit-coupled Bose-Einstein condensations

Xiang-Fa Zhou,[1,2] Zheng-Wei Zhou,[1,2] Congjun Wu,[3] and Guang-Can Guo[1,2]

[1]*Key Laboratory of Quantum Information, University of Science and Technology of China, Chinese Academy of Sciences, Hefei, Anhui 230026, China*

[2]*Synergetic Innovation Center of Quantum Information and Quantum Physics, University of Science and Technology of China, Hefei, Anhui 230026, China*

[3]*Department of Physics, University of California, San Diego, California 92093, USA*

(Received 20 October 2014; published 4 March 2015)

We consider the ground-state properties of the two-component spin-orbit-coupled ultracold bosons subject to a rotationally symmetric in-plane gradient magnetic field. In the noninteracting case, the ground state supports giant vortices carrying large angular momenta without rotating the trap. The vorticity is highly tunable by varying the amplitudes and orientations of the magnetic field. Interactions drive the system from a giant-vortex state to various configurations of vortex lattice states along a ring. Vortices exhibit ellipse-shaped envelopes with the major and minor axes determined by the spin-orbit coupling and healing lengths, respectively. Phase diagrams of vortex lattice configurations are constructed and their stabilities are analyzed.

DOI: 10.1103/PhysRevA.91.033603 PACS number(s): 03.75.Mn, 03.75.Lm, 03.75.Nt, 67.85.Fg

I. INTRODUCTION

Spin-orbit (SO) coupling plays an important role in contemporary condensed matter physics, which is linked with many important effects ranging from atomic structures and spintronics to topological insulators [1–3]. It also provides a new opportunity to search for novel states with ultracold atom gases which cannot be easily realized in condensed matter systems. In the usual bosonic systems, the ground-state condensate wave functions are positive definite, which is known as the "no-node" theorem [4,5]. However, the appearance of SO coupling invalidates this theorem [6]. The ground-state configurations of SO-coupled Bose-Einstein condensations (BEC) have been extensively investigated and a rich structure of exotic phases are obtained including the ferromagnetic and spin spiral condensations [6–9], spin textures of the skyrmion type [6,10–13], and quantum quasicrystals [14], etc. On the experimental side, since the pioneering work in the NIST group [15], it has received a great deal of attention, and further progress has been achieved [16–20]. Searching for novel quantum phases in this highly tunable system is still an ongoing work, both theoretically and practically [21–28], and has been reviewed in Refs. [29–33].

On the other hand, effective gradient magnetic fields have been studied in various neutral atomic systems recently. For instance, it has been shown in Refs. [34,35] that SO coupling can be simulated by applying a sequence of gradient-magnetic-field pulses without involving complex atom-laser coupling. In optical lattices, theoretical and experimental progress shows that SO coupling and spin Hall physics can be implemented without spin-flip process by employing gradient magnetic fields [36,37]. This represents the cornerstone of exploring rich many-body physics using neutral ultracold atoms. Additionally, introducing gradient magnetic fields has also been employed to create various topological defects including Dirac monopoles [38] and knot solitons [39]. It would be very attractive to investigate the exotic physics by combining both SO coupling and the gradient magnetic field together in ultracold quantum gases.

In this work, we consider the SO-coupled BECs subject to an in-plane gradient magnetic field in a two-dimensional (2D) geometry. Our calculation shows that this system supports a variety of interesting phases. The main features are summarized as follows. First, the single-particle ground states exhibit giant-vortex states carrying large angular momenta. It is very different from the usual fast-rotating BEC system, in which the giant-vortex state appears only as metastable states [40,41]. Second, increasing the interaction strength causes the phase transition into the vortex lattice state along a ring plus a giant core. The corresponding distribution in momentum space changes from a symmetric structure at small interaction strengths to an asymmetric one as the interaction becomes strong. Finally, the size of a single vortex is determined by two different length scales, namely, the SO coupling strength together with the healing length. Therefore, the vortex exhibits an ellipse-shaped envelope with the principle axes determined by these two scales. This is different from the usual vortex in rotating BECs [42–47], where an axially symmetric density profile is always favored.

The rest of this article is organized as follows. In Sec. II, the model Hamiltonian is introduced. The single-particle wave functions are described in Sec. III. The phase transitions among different vortex lattice configurations are investigated in Sec. IV. The possible experimental realizations are discussed in Sec. V. Conclusions are presented in Sec. VI.

II. THE MODEL HAMILTONIAN

We consider a quasi-2D SO-coupled BEC subject to a spatially dependent magnetic field with the following Hamiltonian as

$$H = \int d\vec{r}^2 \hat{\psi}(\vec{r})^\dagger \left\{ \frac{\vec{p}^2}{2M} + \Lambda r \left(\cos\theta \hat{r} + \sin\theta \hat{\varphi}\right)\cdot\vec{\sigma} + \frac{1}{2}M\omega^2 r^2 \right\} \hat{\psi}(\vec{r}) + H_{\rm soc} + H_{\rm int}, \quad (1)$$

where $\hat{r} = \vec{r}/r$ with $\vec{r} = (x,y)$, $\vec{\sigma} = (\sigma_x,\sigma_y)$ are the usual Pauli matrices; M is the atom mass; ω is the trapping frequency; Λ is the strength of the magnetic field; and θ denotes the relative angle between the magnetic field and the radial direction $\hat{r}$. Physically, this quasi-2D system can be implemented by imposing a highly anisotropic harmonic trap potential $V_H = \frac{1}{2}M(\omega^2 r^2 + \omega_z^2 z^2)$. When $\omega_z \gg \omega$, atoms are mostly confined in the xy plane, and the wave function along the z axis is determined as a harmonic ground state with the characteristic length $a_z = \sqrt{\hbar/(M\omega_z)}$.

For simplicity, the SO coupling employed below has the following symmetric form as

$$H_{\rm soc} = \int d\vec{r}^2 \hat{\psi}(\vec{r})^\dagger \left[\frac{\lambda}{M}(p_x\sigma_x + p_y\sigma_y)\right]\hat{\psi}(\vec{r})$$

with λ as the SO coupling strength. We note that due to this term the magnetic fields which couple to spin can be employed as a useful method to control the orbit degree of freedom of the cloud. The interaction energy is written as

$$H_{\rm int} = \frac{g_{2D}}{2}\int d\vec{r}^2 \hat{\psi}(\vec{r})^\dagger \hat{\psi}(\vec{r})^\dagger \hat{\psi}(\vec{r})\hat{\psi}(\vec{r}). \quad (2)$$

Here the contact interaction between atoms in bulk is $g = 4\pi\hbar^2 a_s/M$, where a_s is the scattering length. For the quasi-2D geometry that we focus on, the effective interaction strength is modified as $g_{2D} = g_{3D}/(\sqrt{2\pi}a_z)$.

III. SINGLE-PARTICLE PROPERTIES

The physics of Eq. (1) can be illustrated by considering the single-particle properties first. After introducing the characteristic length scale of the confining trap $l_T = \sqrt{\hbar/M\omega}$, the dimensionless Hamiltonian is rewritten as

$$\frac{H_0}{\hbar\omega} = \int d\vec{\rho}^2 \hat{\phi}(\vec{\rho})^\dagger \left\{-\frac{\vec{\nabla}^2}{2} + \beta\rho\,(\cos\theta\hat{r} + \sin\theta\hat{\varphi})\cdot\vec{\sigma} + \alpha\vec{k}\cdot\vec{\sigma} + \frac{1}{2}\rho^2\right\}\hat{\phi}(\vec{\rho}), \quad (3)$$

where $\alpha = \lambda/(M\omega l_T)$ and $\beta = \Lambda l_T/(\hbar\omega)$ are the dimensionless SOC and magnetic field strengths, respectively; the normalized condensate wave function is defined as

$$\phi(\vec{\rho}) = \frac{l_T}{\sqrt{N}}\Psi(\vec{r} = l_T\vec{\rho}),$$

with N being the total number of atoms;

Since the total angular momentum $\hbar j_z = \hbar l_z + \frac{\hbar}{2}\sigma_z$ is conserved for this typical Hamiltonian, we can use it to label the single-particle states. If the magnetic field is along the radial direction, i.e., $\theta = l\pi$, the Hamiltonian also supports a generalized parity symmetry described by $i\sigma_y P_x$, namely

$$[H_0, i\sigma_y P_x] = 0, \quad (4)$$

with P_x being the reflection operation about the y axis satisfying $P_x : (x,y) \to (-x,y)$. Therefore, for given eigenstates $\phi_m = [f(\rho)e^{im\varphi}, g(\rho)e^{i(m+1)\varphi}]^T$ with $j_z = (m + 1/2)$, the above symmetry indicates that these two states $\{\phi_m, (i\sigma_y P_x)\phi_m\}$ are degenerate for $H_0(\theta = l\pi)$. This symmetry is broken when $\theta \neq l\pi$.

Due to the coupling between the real space magnetic field and momentum space SO coupling, the single-particle ground states exhibit interesting properties at large values of α and β. In momentum space, the low-energy state moves to a circle with the radius determined by α. The momentum space single-particle eigenstates break into two bands $\psi^\pm(\vec{k})$ with the corresponding eigenvalues $E^\pm_{\vec{k}}/(\hbar\omega) = \frac{1}{2}(|\vec{k}|^2 \pm 2\alpha|\vec{k}|)$ and eigenstates $\frac{1}{\sqrt{2}}[1, \pm e^{i\theta_k}]^T$, respectively. For the lower band, which we focus on, the spin orientation is $\langle\vec{\sigma}\rangle = (-\cos\theta_{\vec{k}}, -\sin\theta_{\vec{k}})$, which is antiparallel to $\vec{k}$. On the other hand, in the real space, for a large value of β, the potential energy in real space is minimized around the circle with the radius $r/l_T = \beta$ with a spatially dependent spin polarization. Therefore, around this space circle, the local wave vector at a position $\vec{r}$ is aligned along the direction of the local magnetic field to minimize the energy. The projection of the local wave vector along the tangent direction of the ring gives rise to the circulation, and thus the ground state carries large angular momentum m, which is estimated as

$$m \simeq 2\pi\beta\sin\theta/(2\pi/\alpha) = \alpha\beta\sin\theta. \quad (5)$$

Therefore, by varying the angle θ, a series of ground states are obtained with their angular momentum ranging from 0 to $\alpha\beta \gg 1$. This is very different from the usual method to generate a giant vortex, where a fast-rotating trap is needed [42].

For $\beta \gg 1$, the low-energy wave functions mainly distribute around the circle $\rho = \beta$. As shown in Appendix A, the approximate wave functions for the lowest band ($n = 1$) are written as

$$\phi_{n=1,j_z}(\rho,\varphi) \simeq \frac{1}{2\pi^{\frac{3}{4}}\rho^{\frac{1}{2}}} e^{-\frac{(\rho-\beta)^2}{2}} e^{i\rho\alpha\cos\theta} \times \begin{bmatrix} e^{i[m\varphi - \frac{\theta}{2}]} \\ -e^{i[(m+1)\varphi + \frac{\theta}{2}]} \end{bmatrix}, \quad (6)$$

where φ is the azimuthal angle. The corresponding energy dispersion is approximated as

$$E_{n,j_z} \approx n + \frac{1-\alpha^2-\beta^2}{2} + \frac{(j_z - \alpha\beta\sin\theta)^2}{2(\alpha^2\cos^2\theta + \beta^2)}. \quad (7)$$

For given values of α and β, E_{n,j_z} is minimized at $j_z \simeq \alpha\beta\sin\theta$, which is consistent with the above discussion. In the case of $\theta = l\pi$, two states with $m = l$ and $-(l+1)$ are degenerated due to the symmetry defined in Eq. (4). Interestingly, Eq. (7) also indicates that for integer $\alpha\beta\sin\theta = l$, an approximate degeneracy occurs for $m = l$ and $l - 1$.

Figure 1 shows the single-particle dispersion of different angular momentum eigenstates along with the radius β for different values of θ. For $\theta = 0$, the dispersions with different j_z never cross each other [Fig. 1(a)]. The values of j_z for the ground state are always $j_z = \frac{1}{2}$ or $-\frac{1}{2}$ due to the symmetry [Eq. (4)]. When $\theta = \pi/4 \neq 0$, the spectra cross at certain parameter values, and the ground state can be degenerate even without additional symmetries as shown in Fig. 1(b), which is consistent with the above discussions. For $\beta \gg 1$, the probability density of the ground-state single-particle wave function mainly distributes around a ring with $\rho = \beta$. Interestingly, the phase distribution exhibits the typical Archimedean spirals with the equal-phase line satisfying $\rho \sim m\varphi$ (or $\rho \sim (m+1)\varphi$) (see Fig. 2 for details).

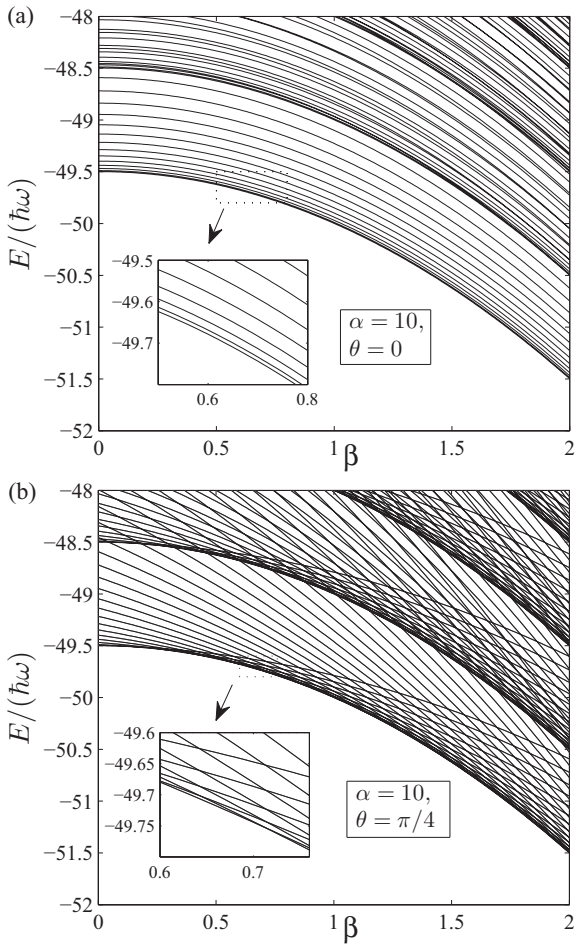

FIG. 1. The single-particle dispersion of the Hamiltonian Eq. (3) with lower energy branch as a function of the reduced magnetic fields β for fixed $\alpha = 10$ and different values of $\theta = 0$ (a) and $\frac{1}{4}\pi$ (b). The inset in panel (b) shows that the ground states crossing for certain values of β at $\theta = \pi/4 \neq 0$, whereas there is no crossing in panel (a) at $\theta = 0$.

IV. PHASE TRANSITIONS INDUCED BY INTERACTION

In this section, we consider the interaction effect which will couple single-particle eigenstates with different values of j_z. It is interesting to consider the possible vortex configura-

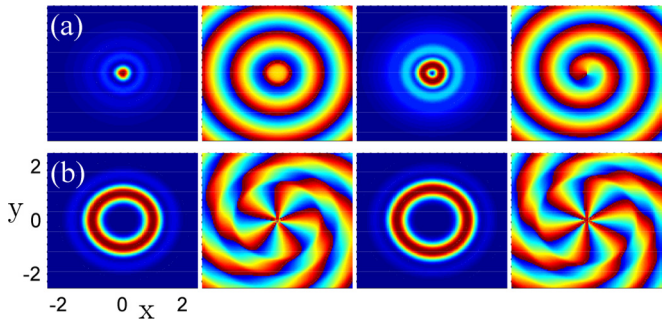

FIG. 2. (Color online) The density and phase profiles of the single-particle ground states for fixed $\alpha = 6$, $\beta = 1$, and different $\theta = \frac{1}{40}\pi$ (a), $\frac{2}{5}\pi$ (b). From left to right: the density and phase profiles for spin-up and spin-down components, respectively.

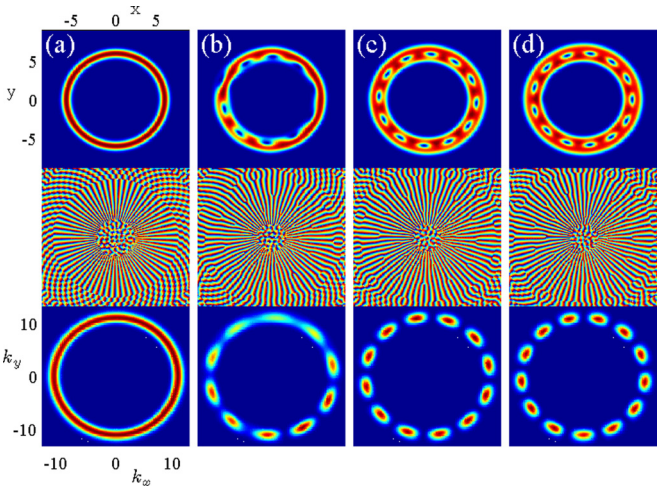

FIG. 3. (Color online) The profiles of the condensate wave functions of the spin-up component for $\alpha = 11$, $\beta = 6$, and $\theta = \frac{\pi}{2}$. The interaction parameters are $g = 15$ (a), 35 (b), 75 (c), and 100 (d), respectively. We note that panels (c) and (d) exhibit similar profiles but with different q. From top to bottom: the density and phase profiles in real space, and the momentum distributions, which mainly are located around the circle $|k| = \alpha$.

tions in various parameter regimes, which have been widely considered in the case of the fast-rotating BECs.

If the dimensionless interaction parameter $g = g_{2D}N/(\hbar\omega l_T^2)$ is small, it is expected that the ground state still remains in a giant-vortex state, which is similar to the noninteracting case. The envelope of the variational wave function is approximated as

$$\phi_{j_z}(\rho,\varphi) \sim \frac{1}{2\pi^{\frac{3}{4}}\sqrt{\sigma\rho}} e^{-\frac{(\rho-\beta)^2}{2\sigma^2}} e^{i\rho\alpha\cos\theta} \begin{bmatrix} e^{i[m\varphi-\frac{\theta}{2}]} \\ -e^{i[(m+1)\varphi+\frac{\theta}{2}]} \end{bmatrix}$$

with σ being the radial width of the condensates. Around a thin ring inside the cloud with the radius ρ, in order to maintain the overall phase factor $e^{im\varphi}$, the magnitude of the local momentum along the azimuth direction is determined by $k_\varphi = m/\rho$. Depending on the width σ of the cloud, the linewidth of k_φ is proportional to $\delta k_\varphi = m\sigma/\beta^2$. In momentum space, this leads to the expansion of the distribution around the ring with $|k| = \alpha$. The increasing of the kinetic energy mainly comes from the term $\hat{E}_\varphi = (j_z/\rho - \alpha\sin\theta)^2/2$, which is estimated as $\langle\hat{E}_\varphi\rangle_{j_z}$. Detailed derivation of various energy contributions can be found in Appendix B.

Increasing the interaction strength g expands the cloud and leads to larger width σ and δk_φ, which makes the above variational state energetically unfavorable. In order to minimize the total energy, the condensates tend to involve additional vortices such that the local momentum mainly distributes around the circle $|k| = \alpha$ with smaller δk_φ. Figs. 3 and 4 show the typical ground-state configurations for selected parameters. The phase accumulations around the inward and outward boundaries of the cloud are $2\pi m_+$ and $2\pi m_-$ respectively. Therefore, there are $q = m_+ - m_-$ vortices involved and distributed symmetrically inside the condensates. Between two nearest vortices, the local wave function can be approximately determined as a plane-wave state. Therefore,

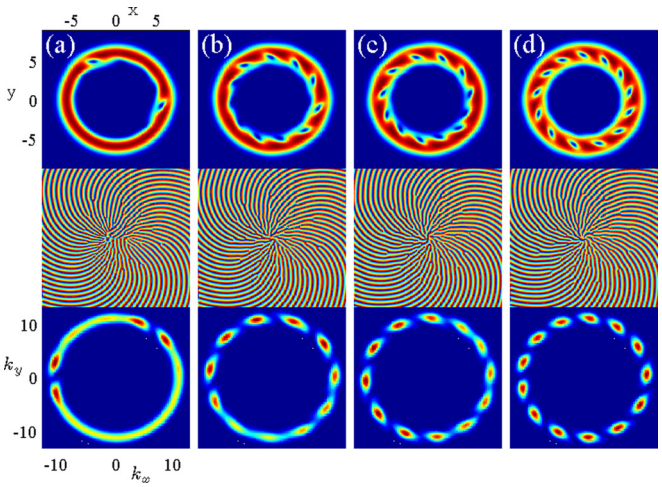

FIG. 4. (Color online) Ground-state profiles of the condensates for $\alpha = 11$, $\beta = 6$, $\theta = \pi/3$ with different interactions $g = 85$ (a), 105 (b), 125 (c), and 145 (d). From top to bottom: density and phase profiles of the spin-up component, and momentum distribution in the lower band along the circle $|k| = \alpha$. The orientation of the ellipse-shaped vortices is determined by θ. See text for details.

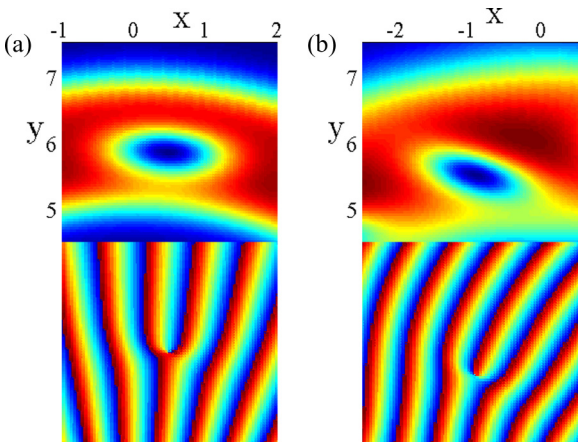

FIG. 5. (Color online) Enlarged density and phase profiles around single vortex. The two panels (a) and (b) are the corresponding parts adapted from Figs. 3(c) and 4(d) respectively.

their corresponding distribution in momentum space is also composed of q peaks located symmetrically around the circle $|k| = \alpha$.

As further increase of the interaction strength, the condensates break into more pieces by involving more vortices. The number of the vortices is qualitatively determined by the competition of the azimuthal kinetic energy and the kinetic energy introduced by the vortices. Specifically, if q vortices locate in the middle of the cloud around the circle $\rho_0 \simeq \beta$, then for the inward part of the condensates with $\rho < \rho_0$, the mean value of the angular momentum can be approximated as $j_{z,-} \approx j_z - q/2$, while for the regime with $\rho > \rho_0$, we have $j_{z,+} \approx j_z + q/2$. The corresponding kinetic energy along the azimuthal direction is modified as

$$\langle \hat{E}_\varphi \rangle = \langle \hat{E}_\varphi \rangle_{j_z} + \frac{q(q - 4\sigma\alpha \sin\theta/\sqrt{\pi})}{8(\beta^2 + \alpha^2 \cos^2\theta)}. \tag{8}$$

This indicates that to make the vortex-lattice state favorable, we must have $(q - 4\sigma\alpha \sin\theta/\sqrt{\pi}) < 0$. In the limit case with $\theta = 0$, this condition is always violated. Therefore, the ground state remains an eigenstate of j_z with $j_z = \pm\frac{1}{2}$ even for large interaction strengths.

We note the vortices display an ellipse-like shape with two main axis, as shown in Fig. 5. The phase profile is twisted, and the constant phase front exhibits a dislocation around vortex cores. Along the direction of local wave vector $\vec{k}$, the vortex density profile is determined by the length scale $2\pi\beta/q \simeq 2\pi m/(q\alpha \sin\theta)$. While perpendicular to the direction of local $\vec{k}$, the vortex profile is dominated by the healing length ξ due to interaction. Therefore, the vortex density distribution is determined by two different length scales in mutually orthogonal directions, which results in ellipse-shaped vortices. Changing the interaction strength and SO coupling alerts the ratio of the two length scales and thus changes the eccentricity of the ellipses. Additionally, changing the angle θ also changes the direction of local magnetic fields and thus modifies the orientation of the vortices, as shown in Figs. 3 and 4.

On the other hand, the introduction of vortices leads to the increase of kinetic energy along the radial direction due to the presence of a domain wall between the two different giant-vortex states around the circle $\rho = \beta$. This can be estimated as $\frac{1}{2\sqrt{2\pi}\sigma\xi} + \frac{q^2}{8\beta^2 \tan^2\theta}$, where $\xi = 1/(2\sqrt{2gn_0})$ is the dimensionless healing length with $n_0 = |\phi_0|^2$ being the bulk density of the clouds (see Appendix B for details). The total energy changing due to the presence of the vortices can be written as

$$\Delta E = \frac{1}{2\sqrt{2\pi}\sigma\xi} + \frac{q^2}{8\beta^2 \tan^2\theta} + \frac{q(q - 4\sigma\alpha \sin\theta/\sqrt{\pi})}{8(\beta^2 + \alpha^2 \cos^2\theta)}. \tag{9}$$

Several interesting features can be extracted from Eq. (9). For fixed parameters g, α, and β, there always exists a critical θ_c such that $\Delta E = 0$ is satisfied. When $\theta < \theta_c$, then $\Delta E > 0$, which indicates that a giant-vortex ground state is always favored. As α increases, θ_c satisfying $\Delta E = 0$ becomes smaller. At $\theta > \theta_c$, the ground state exhibits a lattice-type structure along the ring with a giant-vortex core. The values of q are determined by minimizing ΔE with respect to g, α, and β, respectively. Figure 6 shows θ_c as a function of SO strength α at which the transition from a giant-vortex state to a vortex-lattice state occurs. When α is small, a giant-vortex state is favored for all values of θ. As α increases, θ_c drops quickly initially and decreases much slower when α becomes large, as shown in Fig. 6(a). In Fig. 6(b), it shows that as increasing the interaction g, it is becomes easier to drive the system into the vortex lattice state.

Figure 7 shows the phase diagram in the α-g plane for a fixed $\beta = 6$ for different values of θ. For a fixed α and at small values of g, the system remains a giant-vortex state until g reaches its critical value g_c. When $g > g_c$, the system enters into an intermediate regime in which vortices start to enter into the condensates from boundaries. The momentum distribution also breaks into several disconnected segments. More single quantum vortices are generated in the condensates

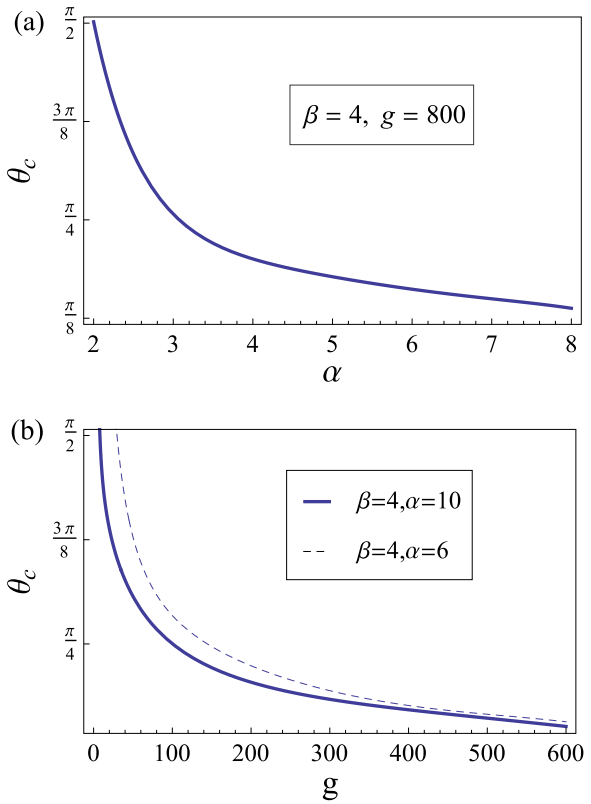

FIG. 6. (Color online) (a) Critical angle θ_c as a function of SO coupling strength α for fixed values of $\beta = 4$ and $g = 800$. (b) θ_c decreases as the increase of interaction parameter g for fixed $\alpha = 10$, 6, and $\beta = 4$.

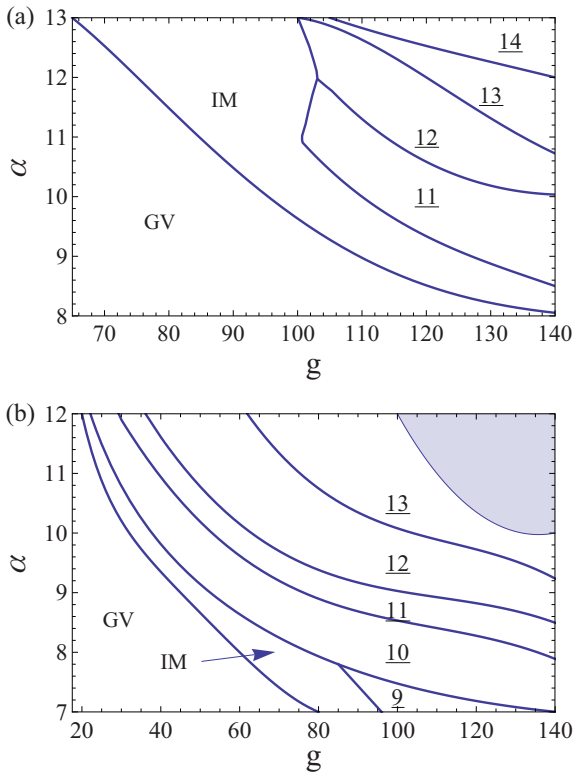

FIG. 7. (Color online) Phase diagram in the α-g plane for $\beta = 6$ with different $\theta = \pi/3$ (a) and $\pi/2$ (b). The number q means that the condensates support a vortex-lattice-type ground state with q momentum peaks along the circle $|k| = \alpha$. The regime with shadow in panel (b) indicates that the ground state shows a multilayer structure with increasing interaction strength. Other phases are defined as follows: GV (giant-vortex state) and IM (intermediate regime).

as the interaction strength further increases. The vortices distribute symmetrically along the ring and separate the condensates into pieces. Between two neighboring vortices, the condensates are approximated by local plane-wave states. The momentum distribution is composed of multiple peaks symmetrically located around the circle $|k| = \alpha$. Increasing g also increases the number of the single quantum vortices q inside the condensates and hence increases the number of peaks in momentum space. For a smaller value $\theta = \pi/3$, the critical g_c is increased, which means that stronger interactions are needed to drive the system into the vortex-lattice states. Interestingly, the intermediate regime is also greatly enlarged. This is consistent with the limit case $\theta = 0$, where the system remains to be a giant-vortex state even in the case of large interaction strength.

More ellipse-shaped vortices are formed as the interaction strength further increases, which are self-organized into a multiple-layered ring structure, as shown in Fig. 8. Around each ring, vortices distributed symmetrically. The number of the vortices between different layers can be distinct due to their different radii. Therefore, the distribution in momentum space becomes asymmetric and exhibits complex multiple-peak structures around the circle $|k| = \alpha$.

V. EXPERIMENTAL CONSIDERATION

The Hamiltonian, Eq. (1), considered above can be dynamically generated on behalf of a series of gradient magnetic pulses [34,35]. Starting with the typical single-particle Hamiltonian $H_s = \frac{p^2}{2M} + \frac{1}{2}M\omega^2 r^2$, in the first time step, we employ a pair of magnetic pulses U_1 and $U_1^\dagger$, defined as

$$U_1 = e^{i\lambda(x\sigma_x + y\sigma_y)/\hbar}, \tag{10}$$

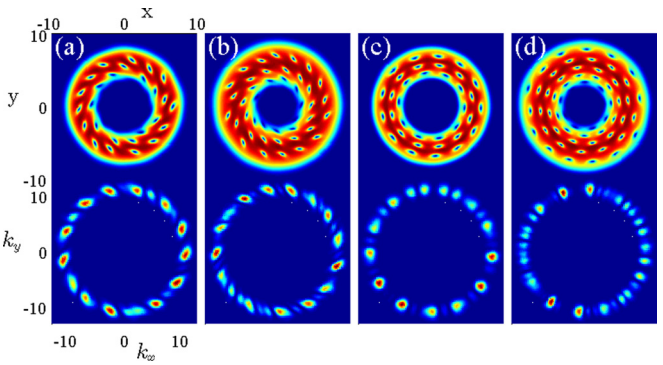

FIG. 8. (Color online) Density and momentum distributions about the ground states of the condensates for $\theta = \pi/3$ with $g = 400$ (a), 1000 (b), and $\theta = \pi/2$ with $g = 400$ (c), 1000 (d). Other parameters are the same as in Fig. 4. We note that since the two spin components share almost the same profiles, only the densities of the spin-up component are shown for simplicity.

at time $t = 2n\tau$, $(2n+1)\tau$ respectively. Second, a typical effective gradient coupling,

$$\Lambda[(x\cos\theta - y\sin\theta)\sigma_x + (y\cos\theta + x\sin\theta)\sigma_y], \quad (11)$$

is applied during the whole time duration $[(2n+1)\tau, 2(n+1)\tau]$. Combining these two time steps, an effective dynamical evolution $U = e^{-iH_0\tau}$ implements the desired dynamics. In practice, the gradient magnetic pulse in the first cycle can be simulated with quadrupole fields as $\vec{B} = (x, y, -2z)$. When the condensates are strongly confined in the xy plane, the influence of the nonzero gradient along the z axis can be neglected. The effective gradient coupling in the second cycle can be implemented with the help of atom-laser coupling. For instance, a standard two-set Raman beams with blue detuning [48] can realize an effective coupling

$$\Omega[\sin(\vec{k}_1\cdot\vec{r})\sigma_x + \sin(\vec{k}_2\cdot\vec{r})\sigma_y], \quad (12)$$

where the wave vectors $\vec{k}_1$ and $\vec{k}_2$ in the xy plane can be chosen as $\vec{k}_1 = k(\cos\theta, -\sin\theta)$ and $\vec{k}_2 = k(\sin\theta, \cos\theta)$. When $2\pi/k$ is much larger than the trap length l_T, the required effective coupling is approximately obtained. Finally, the phases discussed in the context can be detected by monitoring their corresponding density and momentum distributions using the setup of time of flight.

VI. CONCLUDING REMARKS

To summarize, we have discussed the ground-state phase diagram of SO-coupled BECs subject to gradient magnetic fields. Theoretical and numerical analyses indicate that the system supports various interesting vortex physics, including the single-particle giant-vortex states with tunable vorticity, multiple-layered vortex-lattice-ring states, and the ellipse-shaped vortex profiles. Therefore, the combination of SO coupling and the gradient magnetic fields provides a powerful method to engineer various vortex states without rotating the trap. We hope our work will stimulate further research in searching for various novel states in SO-coupled bosons subject to effective gradient magnetic fields.

ACKNOWLEDGMENTS

X.F.Z., Z.W.Z., and G.C.G. acknowledge the support by National Basic Research Program of China (Grants No. 2011CB921200 and No. 2011CBA00200), the Strategic Priority Research Program of the Chinese Academy of Sciences (Grant No. XDB01030000), and NSFC (Grants No. 11004186, No. 11474266, and No. 11174270). C.W. is supported by the NSF DMR-1410375 and AFOSR FA9550-14-1-0168 and also acknowledges the support from the National Natural Science Foundation of China (Grant No. 11328403).

APPENDIX A: SINGLE-PARTICLE EIGENSTATES FOR LARGE β

We start with the dimensionless Hamiltonian

$$\frac{H_0}{\hbar\omega} = \int d\vec{\rho}^2\hat{\phi}(\vec{\rho})^\dagger\left\{-\frac{\vec{\nabla}^2}{2} + \beta\rho(\cos\theta\hat{r} + \sin\theta\hat{\varphi})\cdot\vec{\sigma} + \alpha\vec{k}\cdot\vec{\sigma} + \frac{1}{2}\rho^2\right\}\hat{\phi}(\vec{\rho}). \quad (A1)$$

Since the total angular momentum is conserved, the single-particle eigenstates can be written as $\phi_m = [f(\rho)e^{im\varphi}, g(\rho)e^{i(m+1)\varphi}]^T$ with $j_z = (m+1/2)$. By substituting this wave function into their corresponding Schrödinger equations, we obtain

$$\left\{\frac{\hat{p}_\rho^2}{2} + \frac{j_z^2}{2\rho^2} + \frac{(\rho\sigma_x - \beta)^2}{2} - \alpha\left[\left(\hat{p}_\rho\cos\theta + \frac{j_z}{\rho}\sin\theta\right)\sigma_x + \left(\frac{j_z}{\rho}\cos\theta - \hat{p}_\rho\sin\theta\right)\sigma_y\right] + \frac{j_z\sigma_z}{2\rho^2}\right\}\begin{bmatrix}\tilde{f}(\rho)\\ \tilde{g}(\rho)\end{bmatrix} = E\begin{bmatrix}\tilde{f}(\rho)\\ \tilde{g}(\rho)\end{bmatrix},$$

where $\tilde{f}(\rho) = f(\rho)e^{i\theta/2}$, $\tilde{g}(\rho) = g(\rho)e^{-i\theta/2}$, and $\hat{p}_\rho = -i(\frac{\partial}{\partial\rho} + \frac{1}{2\rho})$ is the momentum operator along the radial direction. For large $\beta \gg 1$, these functions mainly distribute around the circle $\rho = \beta$ in the plane, so we consider the superposition $F^\pm(\rho) = \frac{1}{2}[\tilde{f}(\rho) \pm \tilde{g}(\rho)]$, which satisfies the following approximated equations as

$$\left(\frac{\hat{p}_\rho^2}{2} \mp \alpha\cos\theta\hat{p}_\rho + \frac{j_z^2}{2\rho^2} \mp \alpha\sin\theta\frac{j_z}{\rho} + \frac{\rho^2}{2} \mp \beta\rho\right)F^\pm(\rho) \pm i\alpha\left(\hat{p}_\rho\sin\theta - \frac{j_z}{\rho}\cos\theta\right)F^\mp(\rho) = E_{j_z}F^\pm(\rho).$$

The above equation indicates that to minimize the kinetic energy, we need $\langle\vec{p}_\rho\rangle \simeq \alpha\cos\theta$. Around $\rho = \beta$, we have the approximated solutions as $F^\pm(\rho) \sim H_n(\rho \pm \beta)e^{-(\rho\pm\beta)^2/2}e^{\pm i\alpha\cos\theta\rho}$ with $H_n(r)$ as the usual nth Hermite polynomial. Therefore, F^+ is negligible since we always have $\rho > 0$. The solution now can be written as $\tilde{f}(\rho) \simeq \tilde{g}(\rho) \propto H_n(\rho - \beta)e^{-(\rho-\beta)^2/2}e^{i\alpha\cos\theta\rho}$. So we obtain the approximated wave functions for the lowest band ($n = 1$) as

$$\phi_{n=1,j_z} \simeq \frac{1}{2(\pi)^{\frac{3}{4}}\rho^{\frac{1}{2}}}e^{-\frac{(\rho-\beta)^2}{2}}e^{i\rho\alpha\cos\theta}\begin{bmatrix}e^{i[m\varphi-\frac{\theta}{2}]}\\ -e^{i[(m+1)\varphi+\frac{\theta}{2}]}\end{bmatrix}. \quad (A2)$$

The dispersion is estimated as [49]

$$E_{n,j_z} = n + \frac{1-\alpha^2-\beta^2}{2} + \frac{(j_z - \alpha\beta\sin\theta)^2}{2(\alpha^2\cos^2\theta + \beta^2)}, \quad (A3)$$

which is minimized when $j_z \simeq \alpha\beta\sin\theta$, so for the kinetic term along the tangential direction $\hat{E}_\varphi = (\frac{j_z}{\rho} - \alpha\sin\theta)^2/2$.

APPENDIX B: ENERGY ESTIMATION OF VORTEX LATTICE STATES AROUND THE RING

For weak interaction, the condensates expands along the radial direction as the parameter g is increased. When g is large enough, to lower the kinetic energy, the system tends to involve vortices located around a ring inside the condensates, which separate the wave function into two parts. Inside the vortex ring, the wave function for the spin-up component is approximated as a giant vortex with the phase factor $e^{i2\pi m_-\varphi}$, while outside the ring, the mean angular momentum carried by single particle is approximated as $m_+\hbar$. The difference $q = m_+ - m_-$ represents the vortex number inside the condensates. Therefore the variational ground state can be approximated as

follows:

$$\phi(\rho,\varphi) = \begin{cases} \phi_{j_z-q/2}(\rho,\varphi) \text{ when } \rho \in (0,\beta), \\ \phi_{j_z+q/2}(\rho,\varphi) \text{ when } \rho \in (\beta,\infty). \end{cases} \tag{B1}$$

We also assumes that around the circle $\rho = \beta$, vortices are involved and self-organized to compensate for the phase mismatch so that the whole wave function is well defined. In the general case, we can write the variational wave function as

$$\begin{aligned} \phi(\rho,\varphi) &= \phi_+(\rho)|m_+\rangle + \phi_-(\rho)|m_+\rangle, \\ &= h(\rho)\left[f_+(\rho)|k_+\rangle|m_+\rangle + f_-(\rho)|k_-\rangle|m_-\rangle\right], \end{aligned} \tag{B2}$$

where

$$h(\rho) = \left(\frac{1}{\pi}\right)^{\frac{1}{4}} \frac{1}{\sqrt{2\pi}} \frac{1}{\sqrt{\sigma}} e^{-\frac{(\rho-\beta)^2}{2\sigma^2}},$$

$$f_+(\rho) = \left[\frac{1}{e^{-\frac{\sqrt{2}(\rho-\beta)}{\xi}}+1}\right]^{1/2}, \quad f_-(\rho) = \left[\frac{1}{e^{\frac{\sqrt{2}(\rho-\beta)}{\xi}}+1}\right]^{1/2},$$

$$|k_+\rangle = \frac{e^{ik_+\rho}}{\sqrt{\rho}}, \quad |k_-\rangle = \frac{e^{ik_-\rho}}{\sqrt{\rho}},$$

$$|m_+\rangle = \frac{1}{\sqrt{2}}\begin{bmatrix} e^{i[m_+\varphi-\frac{\theta}{2}]} \\ -e^{i[(m_++1)\varphi+\frac{\theta}{2}]} \end{bmatrix},$$

$$|m_-\rangle = \frac{1}{\sqrt{2}}\begin{bmatrix} e^{i[m_-\varphi-\frac{\theta}{2}]} \\ -e^{i[(m_-+1)\varphi+\frac{\theta}{2}]} \end{bmatrix}.$$

Here we have set $m_\pm = m \pm q/2$. The wave vectors are chosen as $k_\pm = \alpha\cos\theta \pm q/(2\beta\tan\theta)$ such that the local wave vectors are parallel with the local effective magnetic fields. ξ describes the width of the crossover regime of the two different giant-vortex states, which is also equivalent to the healing length. The above wave function contains enough parameters for the following analysis.

The total variational energy of the system can be obtained from

$$E = \langle\hat{E}_\rho\rangle + \langle\hat{E}_\varphi\rangle + E_{\text{int}}, \tag{B3}$$

where $\langle\hat{E}\rangle = \int d\varphi d\rho\rho\phi^\dagger\hat{E}\phi$ with $\hat{E}_\rho = \frac{1}{2}[(\hat{p}_\rho - \alpha\cos\theta)^2 + (\rho-\beta)^2 - (\alpha^2+\beta^2)]$, and $E_{\text{int}} = \frac{g}{2}\int d\varphi d\rho\rho|\phi^\dagger\phi|^2$. By calculating the energy difference of these two wave functions, we can determined the ground-state configuration of the system for giving parameters. For instance, the increase of the kinetic energy around the tangential direction can be estimated as

$$\langle\hat{E}_\varphi\rangle - \langle\hat{E}_\varphi\rangle_{j_z} = \left\langle\frac{q^2}{8\rho^2}\right\rangle_{j_z} + \left\langle\frac{q(j_z-\alpha\sin\theta\rho)}{2\rho^2}(f_+^2 - f_-^2)\right\rangle_{jz}, \tag{B4}$$

where we use $\langle\rangle_{j_z}$ to denote the mean values over the trivial variational function ϕ_{j_z}. Integrating the above formulas, we arrive at the final energy difference as

$$\begin{aligned} \Delta E = E - E_{j_z} &= \frac{1}{4\sqrt{2\pi}\sigma\xi} + \frac{q^2}{8\beta^2\tan^2\theta} \\ &+ \frac{q^2 - 4q\sigma\alpha\sin\theta/\sqrt{\pi}}{8(\beta^2+\alpha^2\cos^2\theta)} + \frac{g\xi}{2\sqrt{2}\beta\pi^2\sigma^2}, \end{aligned} \tag{B5}$$

where we have assumed $\beta \gg \sigma \gg \xi$ to simplify the analysis. Here the first two terms describes the energy increase induced by the kinetic energy along the radial direction $\langle\hat{E}_\rho\rangle$. The third term comes from the different $\langle\hat{E}_\varphi\rangle - \langle\hat{E}_\varphi\rangle_{j_z}$. And finally, the last term denotes the additional interaction energy due to the presence of the domains around the ring $\rho \sim \beta$. For small $\theta \to 0$, we always have $\Delta E > 0$. Therefore, a giant vortex ground state has lower energy. In the opposite case with $\theta \to \pi/2$, ΔE is minimized when $q \simeq 2\alpha\sigma/\sqrt{\pi}$. As the increasing of interaction strength g, the condensate expands with larger σ, which make vortex lattice state energetically favorable. The width of the domain walls can be estimated by minimizing ΔE with respect to ξ, which is determined by the interaction strength as $\xi = \sqrt{\pi^{3/2}\beta\sigma/2g}$. So we have the total energy increase as

$$\Delta E = \frac{1}{2\sqrt{2\pi}\sigma\xi} + \frac{q^2}{8\beta^2\tan^2\theta} + \frac{q^2 - 4q\sigma\alpha\sin\theta/\sqrt{\pi}}{8(\beta^2+\alpha^2\cos^2\theta)}. \tag{B6}$$

The vortex profile can be obtained by considering the variational wave functions around $\rho = \beta$. Specifically, for $\theta = \pi/2$, we have

$$\phi(\rho=\beta,\varphi) \simeq |\phi_0|\sqrt{2}\cos\left(\frac{q}{2}\varphi\right)e^{i(m\varphi-\pi/4)}\begin{bmatrix} 1 \\ -ie^{i\varphi} \end{bmatrix}. \tag{B7}$$

with $|\phi_0| = \frac{h(\beta)}{\sqrt{2\beta}} = [2\pi^{\frac{3}{4}}\sqrt{\sigma\beta}]^{-1}$ being the bulk wave function away from the vortex cores. The position of vortex cores is determined by $\cos(\frac{q}{2}\varphi) = 0$, which results in q independent solutions $\varphi_n = (2n+1)\pi/q$ with $n = 0,1,\ldots,q-1$. To obtain the detailed structure of these vortices, we expand ϕ around these cores as

$$\begin{aligned} \phi(\delta\rho,\delta\varphi) &\simeq |\phi_0|e^{i(m\varphi-\pi/4)}\begin{bmatrix} 1 \\ -ie^{i\varphi} \end{bmatrix}\left(f_+e^{i\frac{q}{2}\varphi} + f_-e^{-i\frac{q}{2}\varphi}\right) \\ &\simeq |\phi_0|e^{i(m\varphi-\pi/4)}\begin{bmatrix} 1 \\ -ie^{i\varphi} \end{bmatrix}(-1)^n i\left(\frac{\delta\rho}{2\xi} + i\frac{\beta\delta\varphi}{\sqrt{2}\beta/q}\right) \end{aligned} \tag{B8}$$

with $\delta\rho = \rho - \beta$ and $\delta\varphi = \varphi - \varphi_n$. Therefore the two spin components share the same density distributions, and vortex profiles are determined by two independent length scales ξ and $2\pi\beta/q$ for the radial and tangential directions respectively [50]. This results in an ellipse-like vortex shape, as shown in Fig. 5.

[1] I. Žutić, J. Fabian, and S. Das Sarma, Rev. Mod. Phys. **76**, 323 (2004).

[2] M. Z. Hasan and C. L. Kane, Rev. Mod. Phys. **82**, 3045 (2010).

[3] X.-L. Qi and S.-C. Zhang, Rev. Mod. Phys. **83**, 1057 (2011).

[4] R. P. Feynman, *Statistical Mechanics: A Set of Lectures* (Addison-Wesley, Reading, MA, 1998).

[5] C. Wu, Mod. Phys. Lett. B **23**, 1 (2009).

[6] C. Wu, I. Mondragon-Shem, and X.-F. Zhou, Chin. Phys. Lett. **28**, 097102 (2011).

[7] T. D. Stanescu, B. Anderson, and V. Galitski, Phys. Rev. A **78**, 023616 (2008).

[8] C. Wang, C. Gao, C. M. Jian, and H. Zhai, Phys. Rev. Lett. **105**, 160403 (2010).

[9] T. L. Ho and S. Zhang, Phys. Rev. Lett. **107**, 150403 (2011).

[10] H. Hu, B. Ramachandhran, H. Pu, and X. J. Liu, Phys. Rev. Lett. **108**, 010402 (2012).

[11] S. Sinha, R. Nath, and L. Santos, Phys. Rev. Lett. **107**, 270401 (2011).

[12] Y. Li, X. Zhou, and C. Wu, arXiv:1205.2162.

[13] T. Kawakami, T. Mizushima, M. Nitta, and K. Machida, Phys. Rev. Lett. **109**, 015301 (2012).

[14] S. Gopalakrishnan, I. Martin, and E. A. Demler, Phys. Rev. Lett. **111**, 185304 (2013).

[15] Y. Lin, R. L. Compton, K. Jiménez-García, J. V. Porto1, and I. B. Spielman, Nature (London) **462**, 628 (2009); Y.-J. Lin, R. L. Compton, A. R. Perry, W. D. Phillips, J. V. Porto, and I. B. Spielman, Phys. Rev. Lett. **102**, 130401 (2009); Y. Lin, K. Jimenez-Garcia, and I. Spielman, Nature (London) **471**, 83 (2011).

[16] J.-Y. Zhang, S.-C. Ji, Z. Chen, L. Zhang, Z.-D. Du, B. Yan, G.-S. Pan, B. Zhao, Y.-J. Deng, H. Zhai, S. Chen, and J.-W. Pan, Phys. Rev. Lett. **109**, 115301 (2012).

[17] P. Wang, Z.-Q. Yu, Z. Fu, J. Miao, L. Huang, S. Chai, H. Zhai, and J. Zhang, Phys. Rev. Lett. **109**, 095301 (2012).

[18] L. W. Cheuk, A. T. Sommer, Z. Hadzibabic, T. Yefsah, W. S. Bakr, and M. W. Zwierlein, Phys. Rev. Lett. **109**, 095302 (2012).

[19] C. Qu, C. Hamner, M. Gong, C. Zhang, and P. Engels, Phys. Rev. A **88**, 021604(R) (2013).

[20] A. J. Olson, S.-J. Wang, R. J. Niffenegger, C.-H. Li, C. H. Greene, and Y. P. Chen, Phys. Rev. A **90**, 013616 (2014).

[21] R. M. Wilson, B. M. Anderson, and C. W. Clark, Phys. Rev. Lett. **111**, 185303 (2013).

[22] V. Achilleos, D. J. Frantzeskakis, P. G. Kevrekidis, and D. E. Pelinovsky, Phys. Rev. Lett. **110**, 264101 (2013).

[23] Y. V. Kartashov, V. V. Konotop, and F. K. Abdullaev, Phys. Rev. Lett. **111**, 060402 (2013).

[24] T. Ozawa and G. Baym, Phys. Rev. Lett. **110**, 085304 (2013).

[25] Y. Deng, J. Cheng, H. Jing, C.-P. Sun, and S. Yi, Phys. Rev. Lett. **108**, 125301 (2012).

[26] Y. Zhang, L. Mao, and C. Zhang, Phys. Rev. Lett. **108**, 035302 (2012).

[27] V. E. Lobanov, Y. V. Kartashov, and V. V. Konotop, Phys. Rev. Lett. **112**, 180403 (2014).

[28] X. Luo, L. Wu, J. Chen, R. Lu, R. Wang, and L. You, arXiv:1403.0767v2; L. He, A. Ji, and W. Hofstetter, arXiv:1404.0970v1; Z.-Q. Yu, Phys. Rev. A **90**, 053608 (2014); W. Han, G. Juzeliūnas, W. Zhang, and W.-M. Liu, *ibid.* **91**, 013607 (2015).

[29] X. Zhou, Y. Li, Z. Cai, and C. Wu, J. Phys. B **46**, 134001 (2013).

[30] J. Dalibard, F. Gerbier, G. Juzeliūnas, and P. Ohberg, Rev. Mod. Phys. **83**, 1523 (2011).

[31] H. Zhai, Int. J. Mod. Phys. B **26**, 1230001 (2012).

[32] V. Galitski and I. B. Spielman, Nature (London) **494**, 49 (2013).

[33] N. Goldman, G. Juzeliūnas, P. Öhberg, and I. B. Spielman, Rep. Prog. Phys. **77**, 126401 (2014).

[34] B. M. Anderson, I. B. Spielman, and G. Juzeliūnas, Phys. Rev. Lett. **111**, 125301 (2013).

[35] Z.-F. Xu, L. You, and M. Ueda, Phys. Rev. A **87**, 063634 (2013).

[36] C. J. Kennedy, Georgios A. Siviloglou, H. Miyake, W. C. Burton, and W. Ketterle, Phys. Rev. Lett. **111**, 225301 (2013).

[37] M. Aidelsburger, M. Atala, M. Lohse, J. T. Barreiro, B. Paredes, and I. Bloch, Phys. Rev. Lett. **111**, 185301 (2013).

[38] V. Pietila and M. Mottonen, Phys. Rev. Lett. **103**, 030401 (2009).

[39] Y. Kawaguchi, M. Nitta, and M. Ueda, Phys. Rev. Lett. **100**, 180403 (2008).

[40] V. Schweikhard, I. Coddington, P. Engels, S. Tung, and E. A. Cornell, Phys. Rev. Lett. **93**, 210403 (2004).

[41] E. J. Mueller and T.-L. Ho, Phys. Rev. Lett. **88**, 180403 (2002).

[42] A. L. Fetter, Rev. Mod. Phys. **81**, 647 (2009).

[43] X. F. Zhou, J. Zhou, and C. Wu, Phys. Rev. A **84**, 063624 (2011).

[44] X.-Q. Xu and J. H. Han, Phys. Rev. Lett. **107**, 200401 (2011).

[45] J. Radić, T. A. Sedrakyan, I. B. Spielman, and V. Galitski, Phys. Rev. A **84**, 063604 (2011).

[46] A. Aftalion and P. Mason, Phys. Rev. A **88**, 023610 (2013).

[47] A. L. Fetter, Phys. Rev. A **89**, 023629 (2014).

[48] X.-J. Liu, K. T. Law, and T. K. Ng, Phys. Rev. Lett. **112**, 086401 (2014).

[49] Since the integral $\int_0^\infty d\rho \frac{j_z^2}{\rho^2} e^{-(\rho-\beta)^2}$ is ill defined when ρ approaches to 0, to obtain the correct dispersion, we need to view $1/(\rho)^2$ as $1/(\rho^*\rho)$ with $1/\rho$ a complex variable with the mean value $1/(\beta + i\alpha\cos\theta)$ for the considered wave function. The result is also checked and compared with numerics, where good agreement is found.

[50] C. J. Pethick and H. Smith, *Bose-Einstein Condensation in Dilute Gases* (Cambridge University Press, Cambridge, UK, 2001).